# Spin-up and spin-down in a half cone: A pathological situation or not?

L. Li,[1] M. D. Patterson,[2] K. Zhang,[1] and R. R. Kerswell[3]
[1]*Department of Mathematics, Exeter University, Exeter EX4 4QL, United Kingdom*
[2]*Department of Architecture & Civil Engineering, Bath University, Bath BA2 7AY, United Kingdom*
[3]*School of Mathematics, Bristol University, Bristol BS8 1TW, United Kingdom*

(Received 9 December 2011; accepted 10 September 2012; published online 12 November 2012)

The spin-up and spin-down of a fluid in a rapidly rotating, fluid-filled, and closed half cone are studied both numerically and experimentally. This unusual set up is of interest because it represents a pathological case for the classical linear theory of Greenspan and Howard [J. Fluid Mech. **17**, 385–404 (1963)] since there are no closed geostrophic contours nor a denumerable set of inertial waves (even a modified theory incorporating Rossby waves by Pedlosky and Greenspan [J. Fluid Mech. **27**, 291–304 (1967)]—relies on geostrophy to leading order). The linearised spin-up/spin-down dynamics in a half cone is found to be dominated by topographical effects which force an ageostrophic leading balance and cause the large-scale starting vorticity to coherently move into the "westward" corner of the half cone for *both* spin-up and spin-down. Once there, viscous boundary layer effects take over as the dominant process ensuring that the spin-up/spin-down time scales conventionally with $E^{-1/2}$, where $E$ is the Ekman number. The numerical coefficient in this time scale is approximately a quarter of that for a full cone when the semi-angle is 30°. Nonlinear spin up from rest is also studied as well as an impulsive 50% reduction in the rotation rate which shows boundary layer separation and small scales. We conclude that spin-up in a rapidly rotating half cone is not pathological because the fluid dynamics is fundamentally the same as that in a container with small topography: in both topography-forced vortex stretching is to the fore. © *2012 American Institute of Physics*. [http://dx.doi.org/10.1063/1.4765333]

## I. INTRODUCTION

How a rotating mass of fluid adjusts from one rotation rate to another imposed by changing boundary conditions is a fundamental issue in rotating fluid mechanics (e.g., see the reviews[1,2]). While the process is well understood for small adjustments in the rotation rate (linear "spin-up" or "spin-down") in containers with closed geostrophic contours,[3–6] many theoretical challenges remain dealing with large-rotation-rate changes (termed nonlinear "spin-up" or "spin-down") and more general geometries. Since the process is ubiquitous in astrophysical and geophysical contexts where extra physics such as compressibility, stratification, and magnetic fields can further complicate the situation, the problem remains one of enduring importance.

The basic spin-up (spin-down) problem is concerned with understanding the fluid adjustment which occurs when the angular velocity $\mathbf{\Omega}$ of a closed container completely filled with a viscous incompressible Newtonian fluid is impulsively changed to $(1+\epsilon)\mathbf{\Omega}$ with $0 < \epsilon$ ($\epsilon < 0$). When $|\epsilon| \ll 1$, the Navier-Stokes equations can be linearised and analytical progress made using matched asymptotic expansions.[3,5] The conclusion of this is that there are three relevant time scales for the adjustment: the inertial time $t_\Omega := 1/\Omega$ for viscous boundary layers to develop, the Ekman time of $t_E := L/\sqrt{\nu\Omega} = E^{-1/2}t_\Omega$—where $E := \nu/(L^2\Omega)$ is the Ekman number, $L$ is a typical length scale of the container, and $\nu$ is the kinematic viscosity of the fluid – over which the change in rotation rate is

 

achieved and the diffusive time $t_\nu := L^2/\nu$ for all residual effects to decay. The analysis decomposes the flow into a secularly evolving geostrophic part and a part which sums up the contribution from the denumerable set of damped oscillatory inertial waves (normal modes) of the system.[5,6] The viscous decay of each part of this decomposition can then be calculated revealing the spin-up (-down) time scale. This appears to work well for geometries with closed geostrophic contours (closed contours of constant depth measured parallel to the rotation axis) and well defined (discrete) inertial modes (e.g., a sphere,[4] Sec. 2.12 of Ref. 6).

Subsequent studies have considered geometries designed to probe various aspects of this theory, e.g., the cylindrical geometry[6–9] where the geostrophic contours are degenerate, containers of uniform depth but non-axisymmetric cross section,[10–12] and containers with obstructions[10,13] or free surfaces.[14] Most notable, however, has been work in a sliced cylinder where no closed geostrophic contours exist;[6,15–17] see also Ref. 18 which considered a rectangular container with a sloping bottom. When the angle of slicing (slope) is small, the disallowed geostrophic mode is replaced by an infinite set of low-frequency, circulation-carrying Rossby waves[15] which are a subset of the inertial waves present. When the slope is not small, van Heijst *et al.*[18] report that the motion is unsteady and irregular in their rectangular container when spinning up from rest. In this situation, Rossby waves, which are defined by having geostrophy as their leading dynamical balance, can no longer be present. Instead, the circulation-carrying duties must now presumably be taken on by the denumerable set of inertial waves with frequencies comparable to the rotation rate (so ageostrophic) which are known to exist in this geometry.[19,20] This, of course, begs the question as to what happens when *both* the geostrophic modes and the inertial waves are absent from a system.

The issue of whether a given geometry hosts a denumerable set of inertial waves is not so easy to address, however. The formally inviscid inertial wave problem has a strange hybrid character: the governing equation is hyperbolic but the boundary conditions are of elliptic type.[6,21] As a result, (inviscid) inertial waves have only been found for a limited number of geometries (e.g., spheres and spheroids,[22–25] cylinders,[26] and planar geometries[27–29]). Adding an inner core to a sphere, for example, destroys many of the waves[30] which can only be recovered when viscosity is added thereby reinstating the elliptic nature of the governing equation.[31] One obviously singular case, however, is the right circular cone which, due to the way inertial waves reflect at boundaries, funnels all wave disturbances into its vertex where they dissipate.[32] As a result, rather than a denumerable set there is a continuum of inertial waves which propagate into the vertex. The subsequent loss of resonant behaviour to periodic forcing has been confirmed in experiments.[33]

The right circular cone, however, is a union of closed (axisymmetric) geostrophic contours which, at least as far as geostrophic flows are concerned, can be treated standardly using the linear theory (e.g., see Eq. (5.17) in Ref. 3). Slicing the cone in half down a plane of reflectional symmetry—creating a "half cone"—changes things completely. There are now no closed geostrophic contours and the cone vertex precludes the existence of a denumerable set of inertial waves. There is then *no* existing linear theoretical framework based upon matched asymptotic expansions to guide understanding of flow. The objective of this investigation is to examine this situation using a combined numerical and experimental approach.

## II. MATHEMATICAL FORMULATION

It is mathematically convenient to employ the two different coordinates – spherical polar coordinates $(r, \theta, \phi)$ with the corresponding unit vectors $(\hat{\mathbf{r}}, \hat{\boldsymbol{\theta}}, \hat{\boldsymbol{\phi}})$ and cylindrical polar coordinates $(s, z, \phi)$ with the corresponding unit vectors $(\hat{\mathbf{s}}, \hat{\mathbf{z}}, \hat{\boldsymbol{\phi}})$ – when describing flows in a half cone. We consider an incompressible viscous fluid filling a volume $V$ in the shape of a half cone of height $H$ defined by $0 \le z = r\cos\theta \le H$, $0 \le \phi \le \pi$, and $0 \le \theta \le \alpha$. Suppose the half cone is rotating uniformly about the axis ($\theta = 0$) (the rotational axis of symmetry of the corresponding full cone) with a constant angular velocity $\hat{\mathbf{z}}\Omega_1$ for $t \le 0$ which is changed impulsively at $t = 0^+$ to a different $\hat{\mathbf{z}}\Omega_2$. The manner in which the initial state approaches a new final state of the rigid-body rotation for

$t > 0$ can be described by the Navier-Stokes equations in the (final) rotating frame with $\hat{\mathbf{z}}\Omega_2$

$$\frac{\partial \mathbf{u}}{\partial t} + \mathbf{u} \cdot \nabla \mathbf{u} + 2\Omega_2 \hat{\mathbf{z}} \times \mathbf{u} = -\frac{1}{\rho}\nabla p + \nu \nabla^2 \mathbf{u}, \tag{1}$$

$$\nabla \cdot \mathbf{u} = 0, \tag{2}$$

where $\nu$ is kinematic viscosity of the fluid, $\rho$ is the fluid density, $p$ is a reduced pressure, and $\mathbf{u}(\mathbf{r}, t)$ is the three-dimensional velocity which is subject to the initial condition

$$\mathbf{u}(\mathbf{r}, 0) = (\Omega_1 - \Omega_2)\hat{\mathbf{z}} \times \mathbf{r} \qquad \text{in} \quad V \tag{3}$$

and the boundary condition $\mathbf{u} = \mathbf{0}$ on $\partial V$. The essence of the spin-up (-down) problem is then to understand how the initial vorticity as viewed from the (final) rotating frame is damped away. The cone semi-angle (or half cone angle) $\alpha$ enters into the problem through the application of the velocity boundary condition. The system is non-dimensionalised using the height $H$ of the half cone as the length scale, $|\Omega_2 - \Omega_1|H$ as the velocity scale, and $\Omega_2^{-1}$ as the unit of time to give

$$\frac{\partial \mathbf{u}}{\partial t} + |Ro|\,(\mathbf{u} \cdot \nabla \mathbf{u}) + 2\hat{\mathbf{z}} \times \mathbf{u} = -\nabla p + E\nabla^2 \mathbf{u}, \tag{4}$$

$$\nabla \cdot \mathbf{u} = 0 \tag{5}$$

together with the initial condition

$$\mathbf{u}(\mathbf{r}, 0) = \frac{\Omega_1 - \Omega_2}{|\Omega_1 - \Omega_2|}\hat{\mathbf{z}} \times \mathbf{r} \qquad \text{in} \quad V \tag{6}$$

and the boundary condition

$$\mathbf{u} = \mathbf{0} \quad \text{on} \quad \partial V. \tag{7}$$

The spin-up/down problem is then characterized by three dimensionless parameters: the angle $\alpha$ of the half cone, the Ekman number $E$ defined as

$$E := \frac{\nu}{\Omega_2 H^2}$$

and the Rossby number $Ro$ given by

$$Ro := \frac{\Omega_2 - \Omega_1}{\Omega_2},$$

where positive (negative) $Ro$ corresponds to the spin-up (spin-down) problem. To keep this study manageable, $\alpha$ is set to $30^\circ$ throughout so that we can concentrate on the effect of varying $Ro$ and $E$ on the spin-up and spin-down processes.

## III. METHODS

The spin-up (or spin-down) problem in a rotating half cone was tackled via both laboratory experiments and fully nonlinear three-dimensional numerical simulations using a finite element method (see the Appendix for details).

In the experiments, a half cone of height 275 mm and radius 156 mm (half-angle $30^\circ$) was used which was manufactured on a Stratasys rapid prototyping machine (a 3D printer). This laid down the plastic material in layers of 0.245 mm which dictated the mechanical tolerance. The system was rotated at angular velocities in the range $[4.21 \times 10^{-2}, 1.151]$ rad/s (0.4–11 rpm) producing Ekman numbers $E$ ranging from $3.14 \times 10^{-4}$ to $1.15 \times 10^{-5}$, respectively. Velocity measurements were obtained at distinct vertical locations within the fluid volume by using a novel particle image velocimetry (PIV) system.[34] This system consisted of a series of low powered lasers that strobe in order to generate horizontal light sheets at distinct vertical locations (data were collected at $z = 0.3$, 0.6, and 0.9), see Figure 1. The lasers were used in conjunction with a Dalsa 4M60 camera that captures images (from above the fluid volume—the camera was supported on a superstructure built

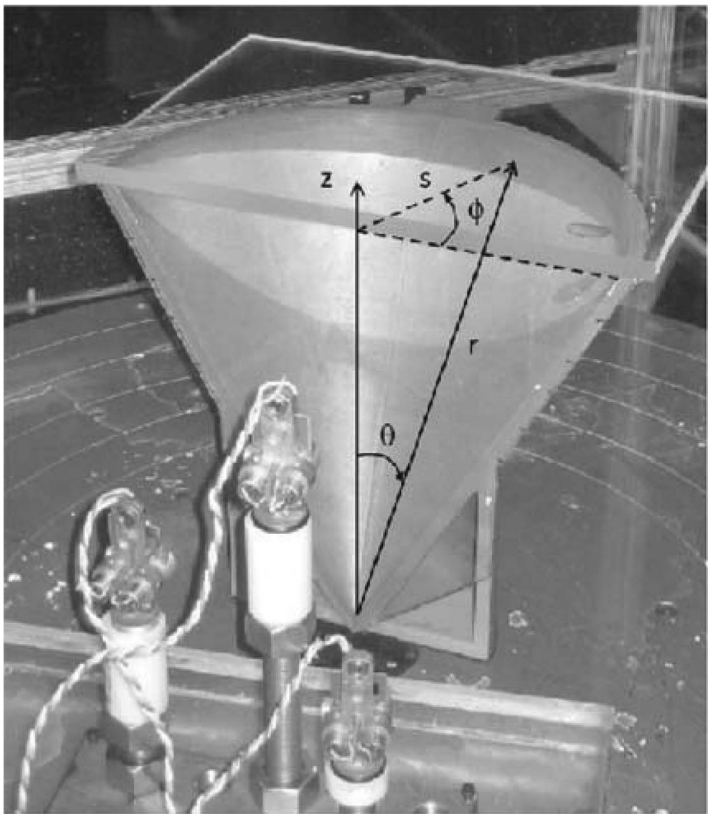


FIG. 1. Photo of the experiment showing the half cone, the coordinate system used in the paper, and the three low powered lasers used to create the light sheets used in the PIV. The half cone has a maximum radius and height of 156 mm and 275 mm, respectively. Note the solid lid which imposes the non-slip boundary condition on the flow at $z = 1$.

on the table) at 30 frames per second with a resolution of $2352 \times 1728$. The PIV system requires that the camera records a frame at the same time that a laser illuminates the flow resulting in the need to strobe the lasers at 30 Hz throughout the flow volume. The fluid volume was seeded with 100 $\mu$m hollow glass spheres that reflect the laser light. Obtaining the correct seeding density and ensuring that the micro spheres are sufficiently close to being neutrally buoyant is essential to the success of this system. In order to achieve this, the fluid was seeded and then left for several hours. All the particles that had sunk or were floating were then removed and the process repeated until sufficient concentration was achieved. Subsequent post processing of the images enabled the development of horizontal velocity fields by tracking the location of the micro spheres.

## IV. RESULTS

### A. Impulsive adjustment

When the rotational speed of the half cone is instantaneously changed at $t = 0$, an impulsive pressure gradient is set up by the boundaries not parallel to the fluid's motion (by definition always present for a non-axisymmetric container). This can be calculated by integrating the momentum equation (4) over a small time interval $t \in [-\epsilon, \epsilon]$ and taking the limit $\epsilon \to 0$ to leave the balance

$$\lim_{\epsilon \to 0} [\mathbf{u}]_{-\epsilon}^{\epsilon} = -\nabla P, \tag{8}$$

where the pressure impulse $P := \lim_{\epsilon \to 0} \int_{-\epsilon}^{\epsilon} p \, dt$. Since $\nabla \cdot \mathbf{u} = 0$, the pressure impulse is a harmonic function ($\nabla^2 P = 0$ in $V$) specified by the non-vanishing gradients on the boundaries where the flow

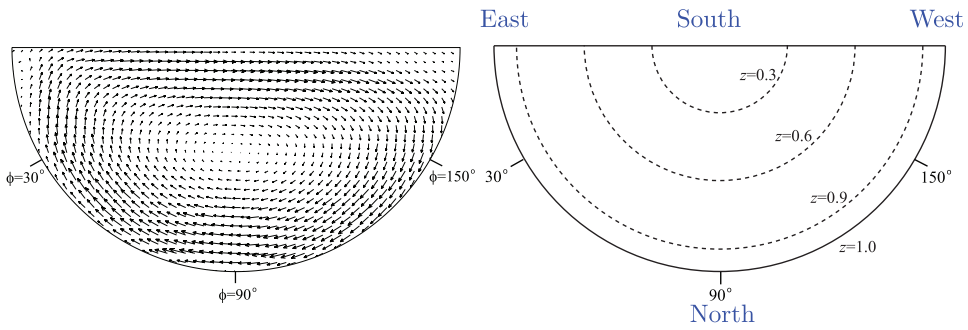


FIG. 2. (Left) The horizontal velocity $\mathbf{u}_{\mathrm{H}} = (u_s, u_\phi)$ at $z = 0.9$, $t = 2$, $\alpha = 30^\circ$, and $E = 5 \times 10^{-5}$ for $Ro = 1.0$ (the flow has negative axial vorticity relative to the impulsively spun-up boundary frame). (Right) The half cone geometry indicating the positions of $30^\circ$, $90^\circ$, and $150^\circ$ as referred to in the text and the crosssectional areas of the slices at $z = 0.3, 0.6$, and 0.9. In the text the top left/right corner is referred to as "east"/"west" in keeping with an oceanographic analogy.

must be immediately corrected,

$$\lim_{\epsilon \to 0}[\hat{\mathbf{n}} \cdot \mathbf{u}]_{-\epsilon}^{\epsilon}|_{\partial V} = -\frac{\Omega_1 - \Omega_2}{|\Omega_1 - \Omega_2|}\hat{\mathbf{n}} \cdot \hat{\mathbf{z}} \times \mathbf{r}|_{\partial V} = -\hat{\mathbf{n}} \cdot \nabla P|_{\partial V}. \tag{9}$$

This is a well-posed problem for $P$ but has no simple solution for the half cone geometry and so is not pursued here (even for the more straightforward 2D semicircle domain a series solution is necessary—see Eq. (15) in Ref. 10). Given $P$, the instantaneously corrected velocity field is then

$$\mathbf{u}(\mathbf{r}, 0) = \frac{\Omega_1 - \Omega_2}{|\Omega_1 - \Omega_2|}\hat{\mathbf{n}} \cdot \hat{\mathbf{z}} \times \mathbf{r} - \nabla P. \tag{10}$$

This makes it clear that the vorticity of the initial field is unchanged by the impulsive correction, a fact that has been verified in many previous studies (e.g., see the discussion surrounding Eq. (10) in Ref. 2). Viscous boundary layers, which take a finite time to form, are the only ways the initial ($t \leq 0$) vorticity field can be brought into alignment with the new boundary motion. How this is done is precisely the spin-up or spin-down process of interest here.

## B. Finite time adjustment

Both numerical simulations and experiments indicate that the flow field at $t = 0^+$ consists of a single symmetric large-scale vortex centred along the $\phi = 90^\circ$ line, see Figure 2. Since the impulsive pressure correction is linear in the pre-adjustment flow field, the structure of this starting vortex is independent of $Ro$—only its amplitude is set by $Ro$ (as viewed relative to the final rotating frame). For later times, both the numerical solutions and experimental data possess the symmetry

$$\mathbf{u}(\mathbf{r}, t; -Ro) = -\mathbf{u}(\mathbf{r}, t; Ro) \tag{11}$$

to a very good approximation for $|Ro| \lesssim 0.05$ indicating a well-defined linear regime of spin-up and spin-down (see Figure 3). In contrast to spin-up/down flows over weak topography, the flow is fully three-dimensional and unsteady due to the $O(1)$ sidewall slope.

### 1. Linear spin-up/spin-down: $|Ro| \leq 0.05$

For small positive or negative Rossby number ($|Ro| \leq 0.05$), the starting vortex is found to migrate to the top right hand corner ($\phi \approx 180^\circ$, see Figure 4) or towards the "west," see Figure 2 ("north" indicates the shallow end of the half cone at $\phi = 90^\circ$ and "south" the deep end at the axis motivated by an oceanographic analogy[15]). In doing so, it shrinks in spatial extent but largely maintains its amplitude. Once pressed in the corner, the dominant process is then damping of the vortex by the Ekman boundary layer on the curved surface near $\phi \approx 180^\circ$. The lack of influence of the top (usually dominant) horizontal Ekman layer is perhaps surprising but unmistakable from the numerical solutions. Figure 4 plotted at $Ro = 0.01$ shows that the vertical motion is polarised

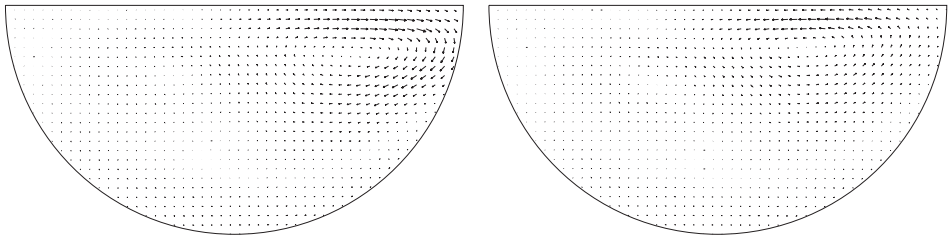

FIG. 3. The horizontal velocity $\mathbf{u}_H = (u_s, u_\phi)$ at $z = 0.9$, $t = 10$, $\alpha = 30^\circ$, and $E = 5 \times 10^{-5}$ for $Ro = 0.05$ (left: max $|\mathbf{u}_H| = 0.35$) and $Ro = -0.05$ (right: max $|\mathbf{u}_H| = 0.37$ ). The similarity of the flows (modulo reversing the arrows) indicates that the spin-up and spin-down flows are still predominantly linear in $Ro$ at $|Ro| = 0.05$ although differences are starting to appear at this value.

into an intense upwelling near the westward corner (the "south" or downslope side of the vortex) and a less intense but broader downwelling below ("north" or upslope of) the moving vortex. Figure 4 hints at a predominantly depth-independent flow but there is clearly a depth-dependent contribution.

To quantify the speed of adjustment, a decay time $T_N$ was defined as being the time by which the kinetic energy of the flow has decreased to $1/N$th of its initial value, that is,

$$\frac{\int_V |\mathbf{u}(\mathbf{r}, T_N)|^2 dV}{\int_V |\mathbf{u}(\mathbf{r}, 0)|^2 dV} = \frac{1}{N}. \tag{12}$$

Figure 5 shows the result of calculating this for $N = 100$ and 1000 over various Ekman numbers in the range $[5 \times 10^{-5}, 5 \times 10^{-3}]$ using the numerical solution at $Ro = 0.005$. Taking $T_{100}$ as

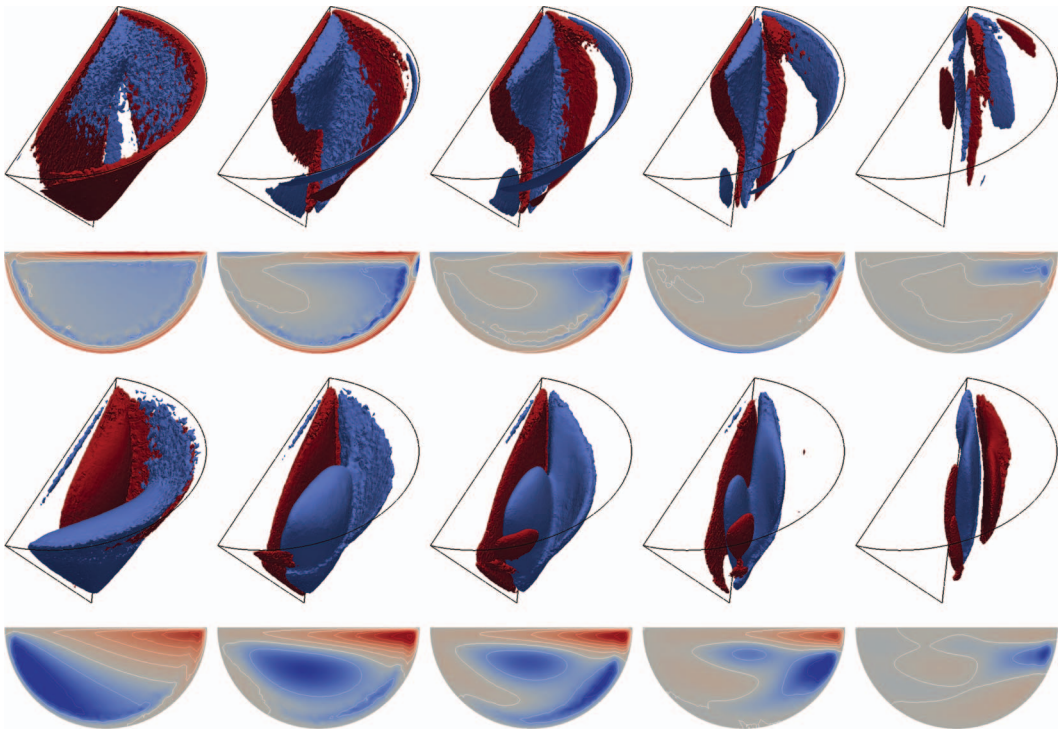

FIG. 4. The isosurfaces (row 1) and contours at $z = 0.6$ (row 2) of vertical vorticity $\omega_z$ for $\alpha = 30^\circ$, $E = 5 \times 10^{-5}$, and $Ro = 0.01$ at $t = 2, 6, 8, 12, 20$ (from left to right). Isosurfaces are $-3$ (blue) and 3 (red); isolines are $-9$ to 21 in steps of 3, with white being 0. The corresponding isosurfaces (row 3) and contours (row 4) of vertical velocity $u_z$, isosurfaces are $-0.03$ (blue) and 0.03 (red); isolines are [–0.15, $-0.1$, $-0.05$, 0, 0.05, 0.1, 0.15, 0.2, 0.25, 0.3, 0.35].

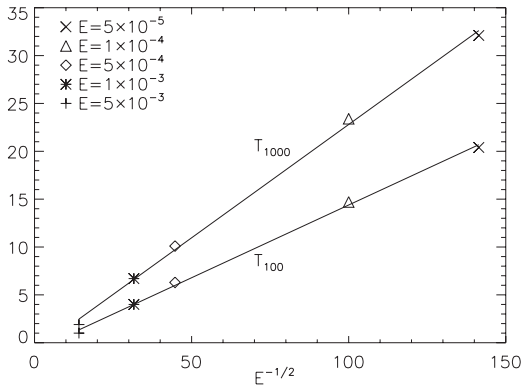


FIG. 5. Numerics: two special decay times, $T_{100}$ and $T_{1000}$ are plotted against $E^{-1/2}$ for the case with $\alpha = 30^\circ$ and $Ro = 0.005$.

the spin-up time, for example, gives a value of $\approx$20 for $E = 5 \times 10^{-5}$, which corresponds to the last vorticity and velocity field shown in Figure 4. Figure 5 shows a clean scaling law $T_N \sim E^{-1/2}$ which is the usual Ekman spin-up result with the coefficient of proportionality depending on $N$ ($dT_N/dE^{-1/2}$ is about 0.2368 for $N = 1000$ and 0.1520 for $N = 100$). Working with the $T_{100}$ result which represents a tenfold reduction in amplitude, an estimate of $\ln 10/0.2368\, E^{1/2} \approx 9.7E^{1/2}$ can be made for the overall viscous damping (spin-up) rate. This can be compared with the linear theory prediction for the equivalent full (axisymmetric) cone defined by $f(r) := -r\cot\alpha \le z \le g(r) := 1$ in the nomenclature of Ref. 3, where $r$ is their cylindrical radius. Their Eq. (5.17) gives the decay (spin-up) rate $\sigma$ as

$$\sigma(r) = \frac{(1+f'^2)^{1/4} + (1+g'^2)^{1/4}}{f+g} E^{1/2} = \frac{\sqrt{2}+1}{1-\sqrt{3}r} E^{1/2}$$

using the fact that $\alpha = 30^\circ$. Reasonably, the centre takes longest to adjust with the smallest viscous damping rate of $1+\sqrt{2} \approx 2.4E^{1/2}$. This is a factor of 4 less than the half cone estimate.

The half-cone is a pathological geometry for the classical Greenspan-Howard spin-up theory because it is not even close[15] to being the union of closed geostrophic contours nor has a denumerable set of inertial waves. The $O(1)$ "topography" presented by the sloping cone side means that the interior of the flow cannot be considered geostrophic to leading order in any way. Instead the Eulerian acceleration term must be retained to disrupt the usual interior inviscid geostrophic balance (and Taylor-Proudman theorem) so that the linearised ($Ro \to 0$) momentum equation (4) is

$$\frac{\partial \mathbf{u}}{\partial t} + 2\hat{\mathbf{z}} \times \mathbf{u} = -\nabla p \tag{13}$$

away from boundaries. The rotation-aligned (or more conveniently termed here as "vertical") component of the vorticity equation—$\hat{\mathbf{z}}.\nabla \times$ (13)—is then simply

$$\frac{\partial \omega_z}{\partial t} = 2\frac{\partial u_z}{\partial z}, \tag{14}$$

where the right hand side is just stretching of the underlying vorticity by a gradient in the vertical velocity. Only this term coupled with the $O(1)$ topography can be responsible for the westward drift of the starting vortex in *both* spin-up and spin-down (viscously driven flow reverses under the transformation $Ro \to -Ro$). The explanation for the westward motion of the starting vortex follows immediately from realising that for spin-up, the starting vortex is anticyclonic (negative) relative to the final boundary frame. In this vortex, the fluid climbs (descends) the topography on the vortex's westerly (easterly) side, see Figure 2. When the fluid climbs topography, $\partial u_z/\partial z < 0$ since $u_z$ has to be positive at depth for the fluid to avoid penetrating the boundary but goes to 0 at the flat half-cone top. Through (14), $\partial \omega_z/\partial t < 0$ at the westerly sides which means that the starting negative vorticity is strengthened to the west. An equivalent (inverted) argument holds for the east side indicating that

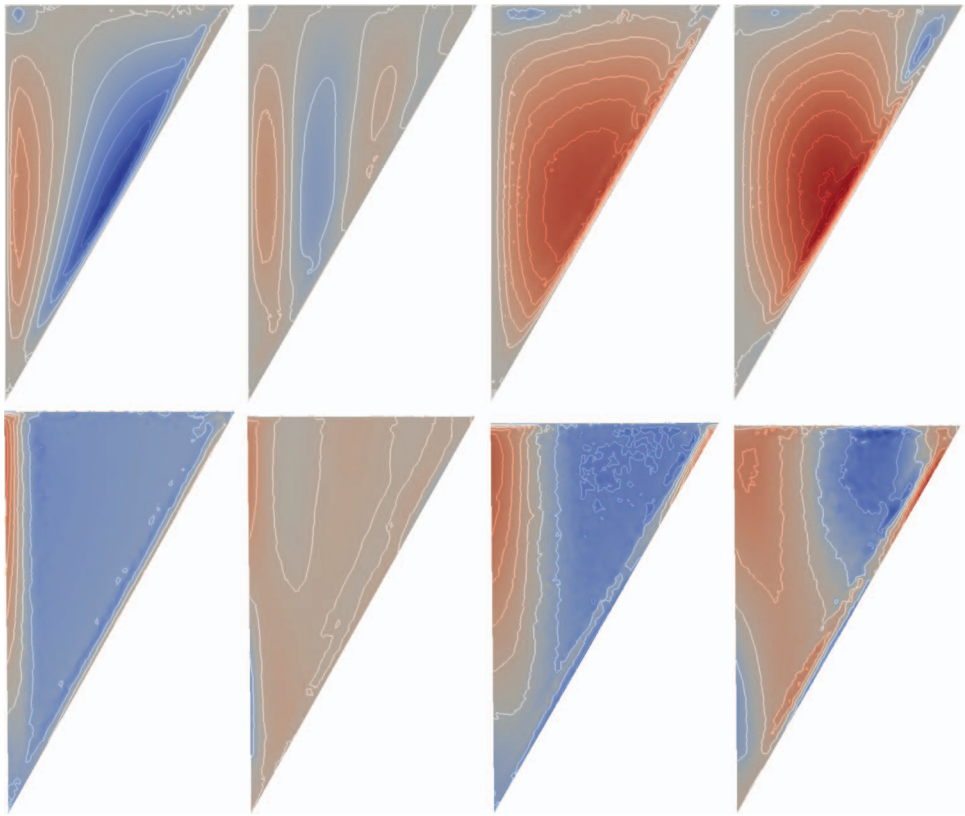

FIG. 6. The vertical velocity $u_z$ (top) and vorticity $\omega_z$ (bottom) for $Ro = 0.01$ and $E = 5 \times 10^{-5}$ on slices with $\phi = 30^\circ$ (left) and $\phi = 170^\circ$ (right) at $t = 2$ and $t = 8$. Contour intervals are 0.03 from dark blue ($u_z = -0.15$) to dark red ($u_z = 0.27$) with white indicating 0. Specific ranges are $u_z \in$ [–0.148, 0.11], $u_z \in$ [–0.049, 0.11], $u_z \in$ [–0.057, 0.212], and $u_z \in$ [–0.08, 0.28], respectively. The contour levels of vertical vorticity are −12 to 24 in steps of 4 with specific ranges $\omega_z \in$ [–4.3, 23.7] (blue/red indicating negative/positive values), $\omega_z \in$ [–5.7, 7.7], $\omega_z \in$ [–6.7, 23.7], and $\omega_z \in$ [–12.9, 19.7].

the vorticity is weakened there. The net result is that the vortex appears to "advect" to the west although advection is a nonlinear effect and excluded. In spin-down, the (positive) surplus starting vorticity causes fluid to descend (climb) in the west (east), so $2\partial u_z/\partial z = \partial \omega_z/\partial t > 0\,(<0)$ and again the vorticity is strengthened in the west and reduced in the east. Slices of the vertical velocity shown in Figure 6 confirm the sign of $\partial u_z/\partial z$ in the east ($\phi = 30^\circ$) and in the west ($\phi = 170^\circ$) at least away from the cone axis (the corresponding migration of vertical vorticity is shown in Figure 6). Itis worth emphasizing that this topographic process is not stretching of the starting vortex (which would be a nonlinear effect) but stretching of the underlying vorticity: the rotation of the system is a fundamental ingredient.

This picture can be further confirmed by examining the full vertical vorticity equation, written as

$$\frac{\partial \omega_z}{\partial t} + \nabla \cdot \mathbf{J} = 0, \tag{15}$$

where

$$\mathbf{J} := |Ro|(\mathbf{u}\omega_z - u_z\boldsymbol{\omega}) - 2u_z\hat{\mathbf{z}} - E\nabla\omega_z \tag{16}$$

is the flux. This makes it clear that there are 3 separate ways to transport the vertical vorticity: (in order from left to right in (16)) advection, stretching of the underlying vorticity and viscous diffusion. Only the latter two are linear and hence incorporated in the Greenspan-Howard spin-up theory. Given the rapid rotation limit $E \ll 1$ of interest here, $\mathbf{J} \cdot \hat{\mathbf{n}}$ was evaluated just outside the curved surface boundary layer to assess which part is most active. Figure 7 shows that the magnitude

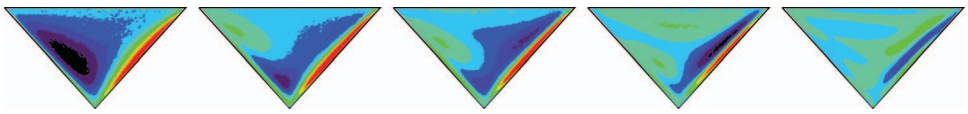

FIG. 7. Temporal evolution of the normal vertical vorticity flux $\mathbf{J}\cdot\hat{\mathbf{n}}E^{-1/2}$ ($\hat{\mathbf{n}}$ points out of the container) evaluated a distance of 0.1 $H$ from the curved sidewall boundary along the boundary normal for $\alpha = 30^\circ$, $E = 5\times10^{-5}$, $Ro = 0.01$; $t = 2$, 6, 8, 12, 20 from left to right. Contour levels are constant across the plots going from −20 (black) to 20 (red) in steps of 4 with the boundary between green and blue indicating 0. In terms of the change in $\omega_z$, $\mathbf{J}\cdot\hat{\mathbf{n}}$ indicates the most active area of the curved boundary layer.

of $\mathbf{J}\cdot\hat{\mathbf{n}}$ is strongly correlated to the position of the vortex and the upwellings and downwellings discussed above. Comparing the size of the vortex stretching term and the viscous term shows that the former dominates (typically by an order of magnitude) confirming that the topography determines the movement of the vortex.

It is tempting to conclude that the linear spin-up/spin-down process in a half cone is a 2-phase process where the starting vortex moves "westwards" across the topography into the west corner before viscous Ekman boundary layers then damp it. However, the temporal evolution of the horizontal kinetic energy at heights $z = 0.3$, 0.6, and 0.9 does not support this, see Figure 8. The horizontal kinetic energy seems to follow a reasonably steady exponential decay (on a time scale $E^{-1/2}$) for $t > 0$ at $z = 0.6$ and $z = 0.9$ rather than showing two distinct behaviours (slopes). (The reason why the $z = 0.3$ line is more undulating than those for $z = 0.6$ or $z = 0.9$ is unclear: the lower velocities there and the smaller averaging area—1/9th) of that at $z = 0.9$, see Figure 2—means it is more sensitive to numerical errors.)

### 2. Nonlinear spin-up/spin-down: $|Ro| > 0.05$

By $Ro = 0.1$ differences between the spin-up flow and the spin-down flow ($Ro = -0.1$) are clearly noticeable to the eye: see the experimental data in Figure 9 and numerical data in Figure 10. The spin-up flow at $Ro = 0.1$ is very similar to that at $Ro = 0.01$ with the starting vortex migrating westwards into the $\phi = 180^\circ$ corner (compare Figures 4 and 10). In contrast for spin-down, the initial vortex moves more southwesterly ending up pressed against the half cone plane near the axis ("south"). The spin-up flow also takes longer to adjust to the new rotation rate than the spin-down flow, a difference confirmed by a systematic survey carried out numerically, see Figure 11 which shows how $T_{100}$ and $T_{1000}$ vary with $Ro$ over the range [–1, 1] at $E = 5\times10^{-5}$. The flatness of the curves near $Ro = 0$ confirm that the linear spin-up/down flow is a very good approximation for finite $Ro$: at $Ro = -0.005$, $T_{100} = 20.45$, and $T_{1000} = 32.11$ as opposed to $T_{100} = 20.41$ and $T_{1000} = 32.13$ at $Ro = 0.005$.

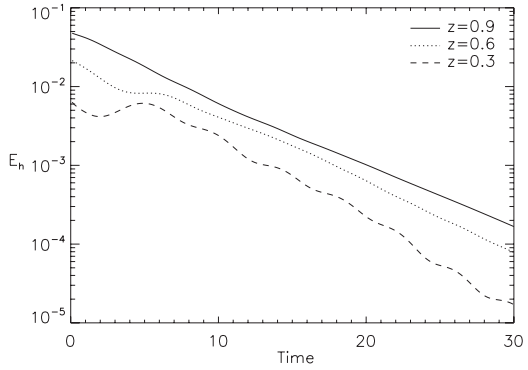


FIG. 8. Numerics: horizontal kinetic energy density $E_h := \int_S |\mathbf{u}_\mathrm{H}|^2 dS/(2S)$, where $\mathbf{u}_\mathrm{H}$ is the velocity perpendicular to the rotation axis is plotted against time for three different planes at $z = 0.9$ (solid line), $z = 0.6$ (dotted line), and $z = 0.3$ (dashed line) with $\alpha = 30^\circ$, $E = 5\times10^{-5}$, and $Ro = -0.01$ (spin-down).

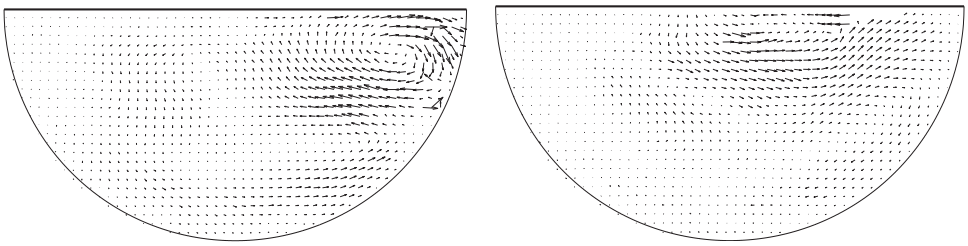

FIG. 9. Experimental measurements of horizontal velocity in the $z = 0.9$ plane for $\alpha = 30^\circ$ and $E = 1.1 \times 10^{-5}$ at $t = 9.1$ for $Ro = 0.1$ (left) and $Ro = -0.1$ (right). The maximum amplitudes (largest arrow) for the horizontal velocity are 0.29 (left) and 0.20 (right)—for calibration the equivalent figures at $t = 1.1$ are 0.32 and 0.35, and 0.26 and 0.13 at $t = 19.9$. The differences shown here illustrate that nonlinear effects are important at $|Ro| = 0.1$.

The flow responses at $Ro = \pm 1$, however, are very different from that near $Ro = 0$ and from each other. We found that the good agreement between the numerical and experimental results for $-0.1 \leq Ro \leq 0.1$ continued up to $Ro = 1$ (spin-up from rest: $\Omega_1 = 0$) as the flow stays relatively large scale and slowly varying: see Figure 12. Now, however, in contrast to the linear response, the starting vortex initially hesitates while it changes shape slightly and then moves a little "eastwards" towards $\phi = 0^\circ$. While doing so, a smaller vortex breaks off and heads towards the westerly corner. The main vortex remains fairly centrally located as it damps. Clearly the nonlinear flux term in $\mathbf{J}$ (Eq. (16)) fights the topographic-driven stretching of the underlying vorticity.

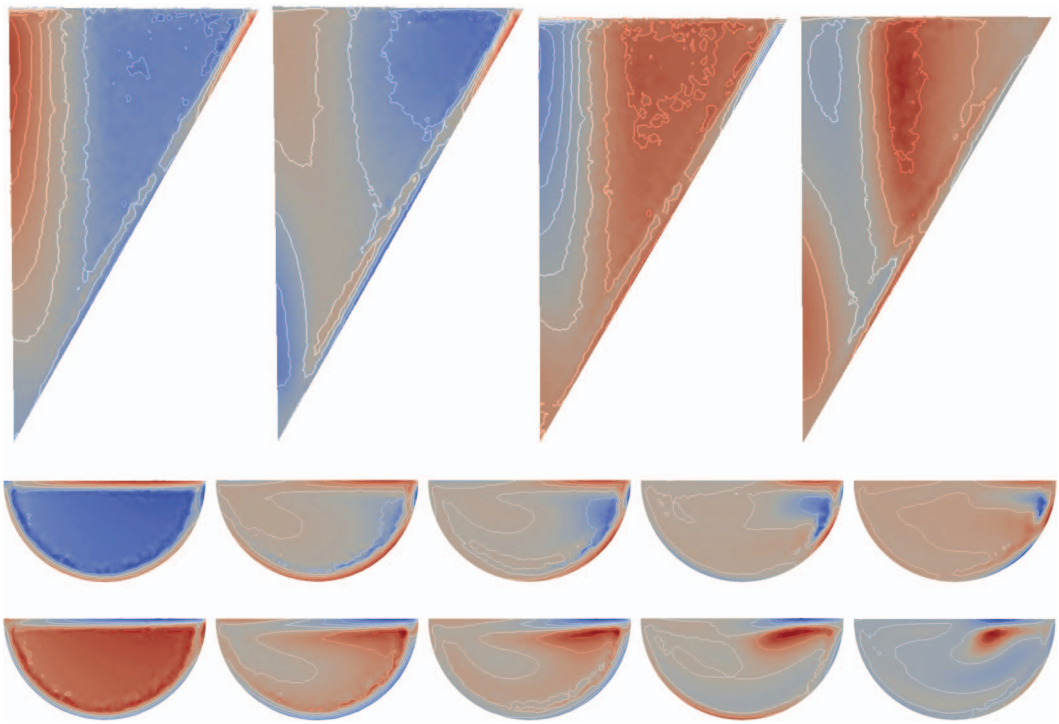

FIG. 10. The vertical vorticity $\omega_z$ at $E = 5 \times 10^{-5}$ on the slice $\phi = 170^\circ$ for $Ro = 0.1$ (row 1, left pair) and $Ro = -0.1$ (row 1, right pair) at $t = 2$ and 8. Contour levels are $-12$ to 24 in steps of 4 (left pair) and $-24$ to 12 in steps of 4 (right pair). The specific ranges are (from left to right) $\omega_z \in$ [–7.1, 24.9] (blue/red indicating negative/positive values), $\omega_z \in$ [–9.2, 26.4], $\omega_z \in$ [–24.8, 6.3], and $\omega_z \in$ [–12.2, 13.3]. The corresponding vertical vorticity $\omega_z$ at $z = 0.6$, $Ro = 0.1$ (row 2) and $Ro = -0.1$ (row 3) at $t = 2, 6, 8, 12, 20$ (from left to right). Isolines are [–9, −6, . . . , 18, 21] with specific ranges [–3.8, 18.2], [–8.6, 15.9], [–7.9, 15.5], [–7.1, 13], [–4.8, 6.5] ordered with time and [–21, −18, . . . , 6, 9] with specific ranges [–21.4, 4.3], [–21.9, 8.1], [21.9, 8.3], [–18.1, 7.4], [–7.8, 4.6], and white means 0.

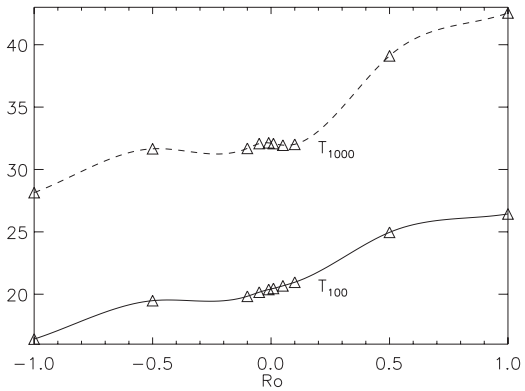


FIG. 11. Numerics: two decay time estimates, $T_{100}$ and $T_{1000}$, are plotted against the Rossby number $Ro$ for $\alpha = 30^\circ$, $E = 5 \times 10^{-5}$.

The flow response for $Ro = -1$ ($\Omega_1 \to \Omega_2 = \frac{1}{2}\Omega_1$) is even more different. Here the flow is impulsively decelerated at $t = 0$ creating an inherently unstable situation. Figure 13 shows that the starting vortex is still visible at $t = 2$ but there is already evidence of boundary layer separation in the east corner ($\phi = 0^\circ$). By $t = 6$, patches of vorticity have broken off from the boundary layer and started to invade the interior to interact with the starting vortex. Figure 13 shows an intense upwelling at $\phi \approx 30^\circ$ between two oppositely signed patches completely absent from the linear spin-down regime. The interior is subsequently small scale, three-dimensional, and rapidly varying. A plot of the horizontal kinetic energy against time (Figure 14) shows how the horizontal energy density of the flow homogenises by about $t \approx 3$ across $z = 0.3$, 0.6, and 0.9 in stark contrast with the linear situation (Figure 8). Spin-down is accomplished by the Ekman boundary layer over the entire curved surface. Surprisingly, despite the more complicated interior flow dynamics, the spin-down time is not significantly lower than the linear case (from Figure 11, $(T_{100}, T_{1000}) \approx (16, 28)$ rather than $\approx (20, 31)$ for $Ro = 0$ at $E = 5 \times 10^{-5}$). Not surprisingly, given that the flow is driven by (boundary layer) instabilities, the experimental results for $Ro = -1$ (Figure 15) cannot be compared directly to the numerical solution beyond early times ($t = 6$ gives a reasonable match but this has degenerated by $t = 12$): differing noise levels and types trigger different effects at varying times. However, the qualitative features are consistent: boundary layer separation occurs near the easterly corner and the interior fills with smaller vortices of differing signs.

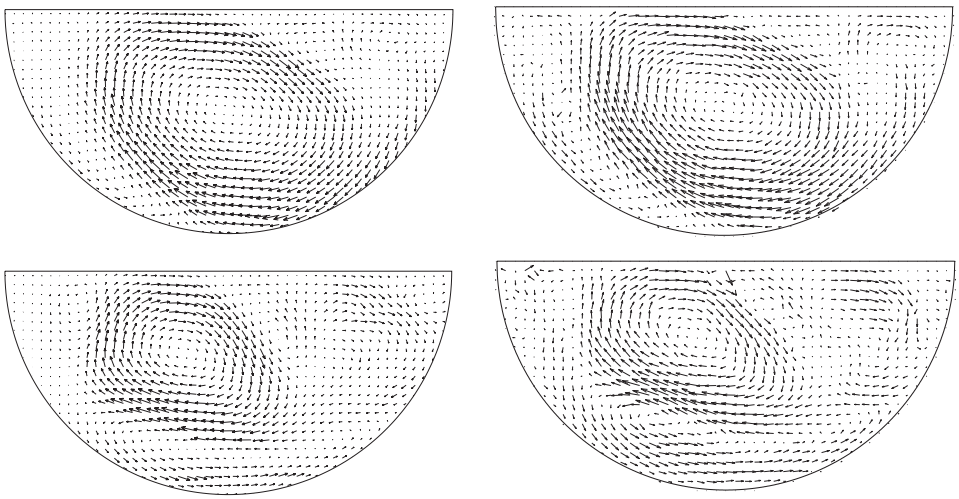

FIG. 12. Comparison of numerical (left) and experimental (right) horizontal velocity data at $Ro = 1$, $E = 5 \times 10^{-5}$, and $z = 0.9$ at $t = 6$ and 12. The maximum horizontal speed at $t = 6$ and 12 is numerically (experimentally) 0.29 (0.30) and 0.21 (0.22).

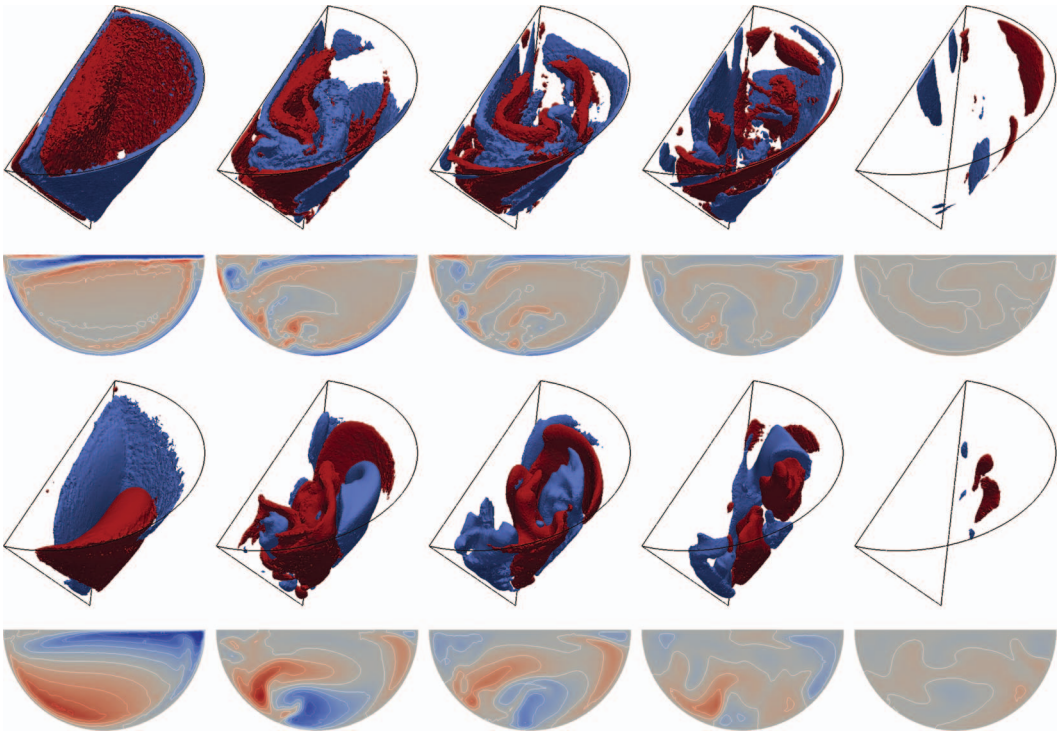

FIG. 13. The isosurfaces (row 1) and contours at $z = 0.6$ (row 2) of vertical vorticity $\omega_z$ for $\alpha = 30^\circ$, $E = 5 \times 10^{-5}$, and $Ro = -1$ at $t = 2$, 6, 8, 12, 20 (from left to right). Isosurfaces are $-2$ (blue) and 2 (red): isolines [–15, $-12$, $-9$, $-6$, $-3$, 0, 3, 6, 9, 12, 15], the white being 0. The corresponding isosurfaces (row 3) and contours at $z = 0.6$ (row 4) of vertical velocity $u_z$, isosurfaces are $-0.04$ (blue) and 0.04 (red): isolines are [–0.25, $-0.2$, $-0.15$, $-0.1$, $-0.05$, 0, 0.05, 0.1, 0.15, 0.2, 0.25].

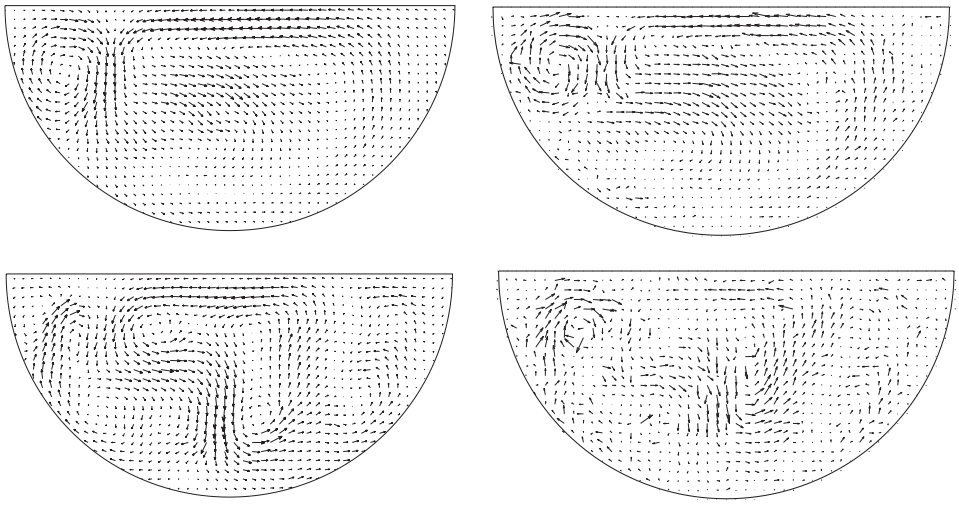

FIG. 14. Comparison of numerical (left) and experimental (right) horizontal velocity data at $Ro = -1$, $E = 5 \times 10^{-5}$, and $z = 0.9$ at $t = 6$ and 12. The maximum horizontal speed at $t = 6$ and 12 is numerically (experimentally) 0.24 (0.23) and 0.12 (0.10).

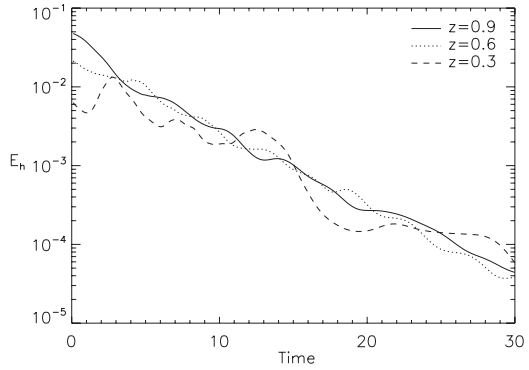


FIG. 15. Numerics: horizontal kinetic energy density $E_h := \int_S |\mathbf{u}_\mathrm{H}|^2 dS/(2S)$, where $\mathbf{u}_\mathrm{H}$ is the velocity perpendicular to the rotation axis is plotted against time for three different planes at $z = 0.9$ (solid line), $z = 0.6$ (dotted line), and $z = 0.3$ (dashed line) with $\alpha = 30^\circ$, $E = 5 \times 10^{-5}$, and $Ro = -1$ (spin-down).

## V. DISCUSSION

The results of this study can be summarised as follows:

- $|Ro| \approx 0.05$ signals the limit of the linear spin-up/spin-down regime where $\mathbf{u}(\mathbf{r}, t; -Ro) = -\mathbf{u}(\mathbf{r}, t; Ro)$ holds to a very good approximation.
- In this linear regime, the starting vortex moves coherently towards the west corner of the half cone regardless of the sign of $Ro$ where it stays while being damped predominantly by the Ekman boundary layer on the sloping surface. The topography is responsible for this apparent motion through vortex stretching of the underlying vorticity of the rotating flow.
- The $Ro = 0.1$ spin-up flow is very similar to the smaller positive $Ro$ flows but for the $Ro = -0.1$ spin-down case, the starting vortex propagates to the south as well, hitting the half cone plane near the axis (the deepest part of the half cone).
- Nonlinear spin-up and spin-down ($Ro = \pm 1$) are significantly different from the (linear) $|Ro| \leq 0.05$ regime. In particular nonlinear (50%) spin-down ($Ro = -1$) shows Ekman boundary separation from the easterly part of the half cone plane and the production of multiple vortices and small scales. Nonlinear spin-up from rest ($Ro = 1$) is stable in comparison with the starting vortex moving slightly eastwards before it damps.
- The relevant linear spin-up/spin-down time scale is the usual $E^{-1/2}/\Omega$. For a half cone of semi-angle of 30°, the spin-up/spin-down process is approximately 4 times faster than in the full cone.

The main finding of this study is the leading order effect of the sloping surface of the half cone on the starting vortex. Because the slope is $O(1)$, the "topography" dictates the vertical velocity of the flow near the boundary completely dominating the Ekman pumping effect which is $O(E^{1/2})$. The horizontal motion topographically determines the vertical velocity which, coupled with a flat upper boundary, then sets up a vertical gradient of vertical velocity. The direction of this gradient sets the sense of vorticity production via stretching of the underlying vorticity. In both the linear spin-up and spin-down scenarios, this effect conspires to "move" the starting vorticity to the west ("along the topography to the right when facing downwards"). Once pressed into the west corner of the half cone, viscous effects then dominate to dampen the surplus vorticity to zero.

The effect of topography on vortices is of fundamental concern in geophysical fluid dynamics and its association with vortex stretching is well known (e.g., the conservation of potential vorticity in the inviscid rotating shallow layer equations). There, the flow is invariably geostrophic to leading order so that the flow is essentially depth-independent. Topography is then a secondary effect which drives variations away from this leading balance. In the quasi-geostrophic equations, for example, it is known that both cyclonic and anticyclonic weak vortices move to the west[35] but they also tend to disintegrate away radiating energy in the form of Rossby waves.[36] We find no evidence of these waves in the half cone except perhaps at very low heights in the cone (the undulating horizontal

kinetic energy curve for $z = 0.3$ in Figure 8) but this seems a secondary effect potentially confined to just ≈3% by volume of the fluid. Pedlosky and Greenspan's[15] modified theory for the spin-up in a cylinder with slightly sloping bottom is similarly built on geostrophy to leading order and draws a related conclusion: the geostrophic spin-up flow is replaced by a set of westward-propagating Rossby waves which are depth-independent to leading order (see also Ref. 17).

The novelty here in the half cone is that the topographic effects are $O(1)$ and hence, the leading interior inviscid dynamics is inherently ageostrophic. Despite this, however, the movement of the starting vorticity seems adequately explained using simple vortex stretching arguments even though the flow is *not* depth-independent in any leading order way. van Heijst *et al.*[18] also recognised the importance of vortex stretching in their study of the spin-up from the rest of flow ($Ro = 1$) in a rectangular container with sloping bottom. However, for a steep slope, they found unsteady and irregular motion throughout the spin-up process and so could not recognise a persistent direction of movement of the starting vortex. Our results suggest that if their experiments were repeated for small $|Ro|$, the starting vortex would propagate coherently to the west side where it should then be damped away by Ekman boundary layer effects.

Finally, in answer to the question posed in this paper's title, the spin-up in a half-cone is certainly pathological from the viewpoint of not fitting into any existing theoretical framework. In particular, the interior is ageostrophic due to the $O(1)$ topography. However, simple vortex stretching arguments prove sufficient to explain the coherent movement of the starting vorticity until it is damped out by the familiarly important Ekman boundary layers leading to the usual spin-up time scale of $E^{-1/2}$. Given this, it seems clear that the fluid dynamics of spin-up in a rapidly rotating half cone is not fundamentally different from that in a container with small topography. As a result of this more important consideration, our final answer is then in the negative.

## ACKNOWLEDGMENTS

L.L. and K.Z. acknowledge the use of the Shanghai supercomputer centre and support by NERC. M.D.P. would like to thank Professor John Wettlaufer for the use of his laboratory facilities at Yale. R.R.K. is grateful to Professor Harvey Greenspan for a chance conversation which stimulated this work.

## APPENDIX: NUMERICAL METHOD

In the temporal discretization of Eqs. (4) and (5), a semi-implicit second-order scheme was employed for time integration. If $t_n = n\Delta t$, $n = 0, 1, 2, \cdots$, is the dimensionless time at step $n$ ($\Delta t$ is the fixed time step), then the second-order backward difference formula

$$\left(\frac{\partial \mathbf{u}}{\partial t}\right)^{n+1} = \frac{3\mathbf{u}^{n+1} - 4\mathbf{u}^{n} + \mathbf{u}^{n-1}}{2\Delta t} + O(\Delta t^2) \tag{A1}$$

was adopted. The nonlinear term $\mathbf{u} \cdot \nabla \mathbf{u}$ at time step $n + 1$ was calculated using a second-order extrapolation scheme

$$(\mathbf{u} \cdot \nabla \mathbf{u})^{n+1} = 2\left(\mathbf{u}^{n} \cdot \nabla \mathbf{u}^{n}\right) - \left(\mathbf{u}^{n-1} \cdot \nabla \mathbf{u}^{n-1}\right) + O(\Delta t^2). \tag{A2}$$

The temporal discretization of Eqs. (4) and (5) was then

$$\left(\frac{\partial \mathbf{u}}{\partial t}\right)^{n+1} + Ro\,(\mathbf{u} \cdot \nabla \mathbf{u})^{n+1} + 2\hat{\mathbf{z}} \times \mathbf{u}^{n+1} = -\nabla p^{n+1} + E\nabla^2 \mathbf{u}^{n+1}, \tag{A3}$$

$$\nabla \cdot \mathbf{u}^{n+1} = 0. \tag{A4}$$

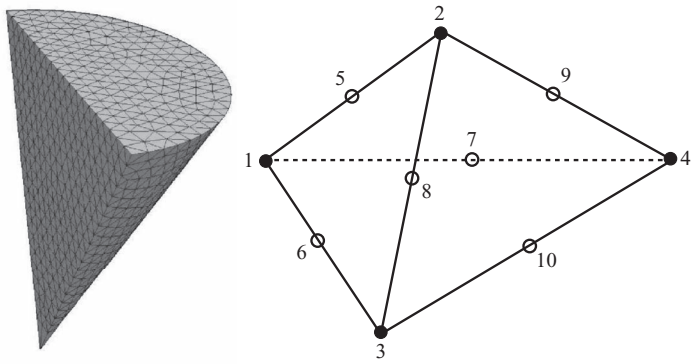


FIG. 16. The left panel shows a schematic of the tetrahedral mesh for the whole half cone. The right panel depicts the node distribution in a typical tetrahedral element: nodes 1–4 for the pressure $p$ while nodes 1–10 for the velocity $\mathbf{u}$.

A tetrahedral mesh, shown in Figure 16, supplied the spatial discretization without any numerical singularities. A Galerkin weighted residual approach was adopted in the finite element formulation of the governing equations (4) and (5). Recalling that $V$ is the volume of the half cone and letting $\mathbf{w_u}$ and $w_p$ be the corresponding weight function for velocity and pressure respectively, the weak formulation of the governing equations, after a standard finite element procedure, then gives rise to

$$\begin{aligned}&\int_V \left(\frac{\partial \mathbf{u}}{\partial t}\right)^{n+1} \cdot \mathbf{w_u} \mathrm{d}V + Ro \int_V (\mathbf{u}\cdot\nabla\mathbf{u})^{n+1} \cdot \mathbf{w_u} \mathrm{d}V \\ &+ \int_V 2\hat{\mathbf{z}} \times \mathbf{u}^{n+1} \cdot \mathbf{w_u} \mathrm{d}V \\ &= -\int_V \nabla p^{n+1} \cdot \mathbf{w_u} \mathrm{d}V - E \int_V \nabla \mathbf{u}^{n+1} \cdot \nabla \mathbf{w_u} \mathbf{d}V, \end{aligned} \tag{A5}$$

$$\int_V \left(\nabla \cdot \mathbf{u}^{n+1}\right) w_p \mathrm{d}V = 0. \tag{A6}$$

A mixed finite element of Hood-Taylor type[37] was adopted and an element-by-element method[38] used in parallelizing the numerical code. In each tetrahedral element, a piecewise quadratic polynomial was employed to approximate the velocity $\mathbf{u}$ while a piecewise linear polynomial is used to approximate the pressure $p$. There are four nodes required for representing the pressure $p$ and ten nodes for $\mathbf{u}$ in each tetrahedron as shown in Figure 16. For a typical $k$th tetrahedral element, the approximation for the velocity $\mathbf{u}$ and pressure $p$ are given by

$$\mathbf{u}^{(k)} = \sum_{j=1}^{10} \mathbf{u}_j^{(k)} N_j^{(k)}, \qquad p^{(k)} = \sum_{j=1}^{4} p_j^{(k)} L_j^{(k)},$$

where $\mathbf{u}_j^{(k)}$ and $p_j^{(k)}$ are the values of $\mathbf{u}$ and $p$ at the node $j$ respectively, and $L_j^{(k)} (j = 1, \ldots, 4)$ are the volume coordinates for the $k$th tetrahedron. The quadratic shape functions $N_j^{(k)}$ are defined as

$$\begin{aligned} N_1^{(k)} &= L_1^{(k)}(2L_1^{(k)} - 1), \qquad N_2^{(k)} = L_2^{(k)}(2L_2^{(k)} - 1), \\ N_3^{(k)} &= L_3^{(k)}(2L_3^{(k)} - 1), \qquad N_4^{(k)} = L_4^{(k)}(2L_4^{(k)} - 1), \\ N_5^{(k)} &= 4L_1^{(k)}L_2^{(k)}, \quad N_6^{(k)} = 4L_1^{(k)}L_3^{(k)}, \quad N_7^{(k)} = 4L_1^{(k)}L_4^{(k)}, \\ N_8^{(k)} &= 4L_2^{(k)}L_3^{(k)}, \quad N_9^{(k)} = 4L_2^{(k)}L_4^{(k)}, \quad N_{10}^{(k)} = 4L_3^{(k)}L_4^{(k)}, \end{aligned}$$

where $L_j^{(k)}$ and $N_j^{(k)}$ have the following properties

$$\sum_{j=1}^{4} L_j^{(k)} = 1, \qquad \sum_{j=1}^{10} N_j^{(k)} = 1.$$

In the Galerkin finite element method used in our simulation, the weight functions are selected to be the same as the corresponding shape functions. Applying the finite element scheme to each tetrahedron, we obtain a system of equations for $\mathbf{u}_j^k$ and $p_j^k$ which are solved by an iterative method.

The code was validated by attempting to reproduce an exact solution, $\mathbf{u}_{exa}(\mathbf{r}, t)$ and $p_{exa}(\mathbf{r}, t)$, that satisfies the equations

$$\frac{\partial \mathbf{u}}{\partial t} + \mathbf{u} \cdot \nabla \mathbf{u} + 2\hat{\mathbf{z}} \times \mathbf{u} + \nabla p = E\nabla^2 \mathbf{u} + \mathbf{f}(\mathbf{r}, t), \tag{A7}$$

$$\nabla \cdot \mathbf{u} = 0, \tag{A8}$$

subject to the non-slip boundary condition

$$\hat{\mathbf{n}} \cdot \mathbf{u} = \hat{\mathbf{n}} \times \mathbf{u} = 0, \tag{A9}$$

with a function $\mathbf{f}(\mathbf{r}, t)$ prescribed. For a half cone with $\alpha = 30^\circ$, we have chosen the exact solution given by $p_{exa}(\mathbf{r}, t) = 0$ and

$$\mathbf{u}_{exa}(\mathbf{r}, t) = \nabla \times [\mathbf{r} T(\mathbf{r}) \cos 2\pi t], \tag{A10}$$

where

$$T(\mathbf{r}) := \left( \frac{z}{\sqrt{3}} - \sqrt{x^2 + y^2} \right)^2 z^2 (1 - z)^2 \cos(2\pi y) \sin^2(\pi x)$$

together with the corresponding $\mathbf{f}(\mathbf{r}, t)$ determined by the Eq. (A7).

The nonlinear equations (A7) and (A8) with the prescribed $\mathbf{f}(\mathbf{r}, t)$ was then integrated forward in time starting with the initial condition

$$\mathbf{u}(t = 0) = \mathbf{u}_{exa}(\mathbf{r}, t = 0). \tag{A11}$$

If the nonlinear half-cone code is correct and accurate, a numerical solution, $\mathbf{u}_{num}(\mathbf{r}, t)$, should be produced such that the difference between $\mathbf{u}_{num}(\mathbf{r}, t)$ and $\mathbf{u}_{exa}(\mathbf{r}, t)$ is small. For measuring the accuracy of the numerical solution, we adopted the following error norms (in both space and time)

$$||\mathbf{u}_{num} - \mathbf{u}_{exa}|| = \sqrt{\frac{1}{2V} \int_0^{t_{\max}} \int_V |\mathbf{u}_{num} - \mathbf{u}_{exa}|^2 dV dt},$$

$$||p_{num} - p_{exa}|| = \sqrt{\frac{1}{2V} \int_0^{t_{\max}} \int_V |p_{num} - p_{exa}|^2 dV dt},$$

where $V$ denotes the volume of the half cone and $t_{\max} = 1$. Four nonlinear simulations were performed at different levels of the finite element mesh for a fixed Ekman number $E = 10^{-4}$, the results of which are shown in Table I. Also displayed in Table I are the details of typical element size $h$, the

TABLE I. The accuracy of nonlinear numerical simulation and the relevant information for finite element tetrahedral meshes employed in simulations with $\Delta t_0 = 10^{-3}$ and $h_0 = 0.018$.

| $h$ | $\Delta t$ | $\|\|u_{num} - u_{exa}\|\|$ | $\|\|p_{num} - p_{exa}\|\|$ | Nodes | Elements | Unknowns |
|---|---|---|---|---|---|---|
| $\approx 1.25h_0$ | $1.25\Delta t_0$ | $3.6024 \times 10^{-10}$ | $9.5529 \times 10^{-11}$ | 20 867 | 11 902 | 37 452 |
| $\approx h_0$ | $\Delta t_0$ | $1.2275 \times 10^{-10}$ | $7.4770 \times 10^{-11}$ | 46 192 | 29 213 | 104 034 |
| $\approx h_0/2$ | $\Delta t_0/2$ | $7.5723 \times 10^{-11}$ | $7.0907 \times 10^{-11}$ | 340 146 | 232 954 | 901 290 |
| $\approx h_0/4$ | $\Delta t_0/4$ | $7.4972 \times 10^{-11}$ | $7.0518 \times 10^{-11}$ | 2 599 107 | 1 863 576 | 7 474 255 |

size of time-integrating step $\Delta t$, and the total number of nodes and unknowns. Excellent agreement is found between the computed nonlinear numerical solution and the constructed exact solution.


[1] E. R. Benton and A. Clark, "Spin-up," Annu. Rev. Fluid Mech. **6**, 257–280 (1974).
[2] P. W. Duck and M. R. Foster, "Spin-up of homogeneous and stratified fluids," Annu. Rev. Fluid Mech. **33**, 231–263 (2001).
[3] H. P. Greenspan and L. N. Howard, "On the time-dependent motion of a rotating fluid," J. Fluid Mech. **17**, 385–404 (1963).
[4] H. P. Greenspan, "On the transient motion of a contained rotating fluid," J. Fluid Mech. **20**, 673–696 (1964).
[5] H. P. Greenspan, "On the general theory of contained rotating fluid motions," J. Fluid Mech. **22**, 449–462 (1965).
[6] H. P. Greenspan, *The Theory of Rotating Fluids* (Cambridge University Press, Cambridge, England, 1968), 327 pp.
[7] E. H. Wedemeyer, "The unsteady flow within a spinning cylinder," J. Fluid Mech. **20**, 383–399 (1964).
[8] P. D. Weidman, "On the spin-up and spin-down of a rotating fluid, Part 2. Measurements and stability," J. Fluid Mech. **77**, 709–735 (1976).
[9] W. B. Watkins and R. G. Hussey, "Spin-up from rest in a cylinder," Phys. Fluids **20**, 1596–1604 (1977).
[10] G. J. F. van Heijst, "Spin-up phenomena in non-axisymmetric containers," J. Fluid Mech. **206**, 171–191 (1989).
[11] G. J. F. van Heijst, P. A. Davies, and R. G. Davis, "Spin-up in a rectangular container," Phys. Fluids **2**, 150–159 (1990).
[12] J. A. van de Konijnenberg, "Spin-up in non-axisymmetric containers," Ph.D. dissertation (Eindhoven University of Technology, Eindhoven, The Netherlands, 1995), 156 pp.
[13] J. A. van de Konijnenberg, T. L. Wessels, and G. J. F. van Heijst, "Spin-up in a circular tank with a radial barrier," Phys. Fluids **8**, 2048–2059 (1996).
[14] H. Goller and T. Ranov, "Unsteady rotating flow in a cylinder with a free surface," ASME J. Basic Eng. **90**, 445–454 (1968).
[15] J. Pedlosky and H. P. Greenspan, "A simple laboratory model of the oceanic circulation," J. Fluid Mech. **27**, 291–304 (1967).
[16] R. C. Beardsley, "A laboratory model of wind-driven ocean circulation," J. Fluid Mech. **38**, 255–271 (1969).
[17] J. A. van de Konijnenberg, V. Naulin, J. J. Rasmussen, B. Stenum, and G. J. F. van Heijst, "Linear spin-up in a sliced cylinder," Geophys. Astrophys. Fluid Dyn. **92**, 84–114 (2000).
[18] G. J. F. van Heijst, L. R. M. Maas, and C. W. M. Williams, "The spin-up of fluid in a rectangular container with a sloping bottom," J. Fluid Mech. **265**, 125–159 (1994).
[19] A. M. M. Manders and L. R. M. Maas, "Observations of inertial waves in a rectangular basin with one sloping boundary," J. Fluid Mech. **493**, 59–88 (2003).
[20] A. M. M. Manders and L. R. M. Maas, "On the three-dimensional structure of the inertial wave field in a rectangular basin with one sloping boundary," Fluid Dyn. Res. **35**, 1–21 (2004).
[21] H. Poincare, "Sur léquilibre d'une masse fluide animée d'un mouvement de rotation," Acta Math. **7**, 259–380 (1885).
[22] G. H. Bryan, "The waves on a rotating liquid spheroid of finite ellipticity," Philos. Trans. R. Soc. London, Ser. A **180**, 187–219 (1889).
[23] M. D. Kudlick, "On transient motions in a contained, rotating fluid," Ph.D. dissertation (Mathematics Department, MIT, 1966).
[24] K. Zhang, P. Earnshaw, X. Liao, and F. H. Busse, "On inertial waves in a rotating fluid sphere," J. Fluid Mech. **437**, 103–119 (2001).
[25] K. Zhang, X. Liao, and P. Earnshaw, "On inertial waves and oscillations in a rapidly rotating spheroid," J. Fluid Mech. **504**, 1–40 (2004).
[26] Lord Kelvin, "Vibrations of a columnar vortex," Philos. Mag. **10**, 155–168 (1880).
[27] K. Zhang and P. H. Roberts, "Thermal inertial waves in a rotating fluid layer: Exact and asymptotic solutions," Phys. Fluids **9**, 1980–1987 (1997).
[28] R. M. Mason and R. R. Kerswell, "Chaotic dynamics in a strained rotating flow: A precessing plane fluid layer," J. Fluid Mech. **471**, 71–106 (2002).
[29] L. R. M. Maas, "On the amphidromic structure of inertial waves in a rectangular parallelepiped," Fluid Dyn. Res. **33**, 373–401 (2003).
[30] W. V. R. Malkus, "Hydromagnetic planetary waves," J. Fluid Mech. **28**, 793–802 (1967).
[31] M. Rieutord and L. Valdettaro, "Inertial waves in a rotating spherical shell," J. Fluid Mech. **341**, 77–99 (1997).
[32] H. P. Greenspan, "On the inviscid theory of rotating fluids," Stud. Appl. Math. **48**, 19–28 (1969).
[33] R. C. Beardsley, "An experimental study of inertial waves in a closed cone," Stud. Appl. Math. **49**, 187–196 (1970).
[34] M. D. Patterson and J. S. Wettlaufer, "Scanned multi-LED illumination for volumetric PIV," Rev. Sci. Instrum. **81**(9), 096101 (2010).
[35] J. Bjerknes and J. Holmboe, "On the theory of cyclones," J. Meteorol. **1**, 1–22 (1944).
[36] G. R. Flierl, "The application of linear quasi-geostrophic dynamics to Gulf Stream rings," J. Phys. Oceanogr. **7**, 365–379 (1977).
[37] P. Hood and C. Taylor, "Navier-Stokes equations using mixed interpolation," in *Finite Element Methods in Flow Problems*, edited by J. T. Oden, O. C. Zienkiewicz, R. H. Gallagher, and C. Taylor (UAH, Huntsville, 1974), pp. 57–66.
[38] K. Chan, K. Zhang, L. Li, and X. Liao, "A new generation of convection-driven spherical dynamos using EBE finite element method," Phys. Earth Planet. Inter. **163**, 251–265 (2007).